



# Hierarchically porous, N-defect enriched C-nanosheets boost the H<sub>2</sub>S selective oxidation to elemental sulfur

Shiyan Li<sup>a,b,1</sup>, Hongquan Fu<sup>c,1</sup>, Xingshuai Zhang<sup>a</sup>, Xu Liu<sup>a</sup>, Giulia Tuci<sup>d</sup>,  
Giuliano Giambastiani<sup>d</sup>, Cuong Pham-Huu<sup>e</sup>, Yuefeng Liu<sup>a,\*</sup>

<sup>a</sup> Dalian National Laboratory for Clean Energy, Dalian Institute of Chemical Physics, Chinese Academy of Sciences, 457 Zhongshan Road, Dalian 116023, China

<sup>b</sup> University of Chinese Academy of Sciences, Beijing 100049, China

<sup>c</sup> College of Chemistry and Chemical Engineering, Chemical Synthesis and Pollution Control Key Laboratory of Sichuan Province, China West Normal University, Nanchong, Sichuan 637000, China

<sup>d</sup> Institute of Chemistry of OrganoMetallic Compounds, ICCOM-CNR and Consorzio INSTM, Via Madonna del Piano 10, 50019 Florence, Italy

<sup>e</sup> Institute of Chemistry and Processes for Energy, Environment and Health (ICPEES), UMR 7515 CNRS-University of Strasbourg, 25 rue Becquerel, 67087 Strasbourg Cedex 02, France

## ARTICLE INFO

### Keywords:

Carbon nanomaterials  
Interconnected pores  
High mass diffusion dynamics  
H<sub>2</sub>S selective oxidation  
NaNO<sub>3</sub> as sacrificial template/porogen

## ABSTRACT

H<sub>2</sub>S selective oxidation to elemental sulfur (S<sub>8</sub>) is a typical reaction where the mass product diffusion (e.g., S<sub>8</sub>) through the catalytic bed is crucial as well as the reagents accessibility (e.g., H<sub>2</sub>S, O<sub>2</sub>) to the active sites. The NaNO<sub>3</sub>-assisted pyrolysis of polyacrylamide was applied to synthesize defect-enriched N-doped carbon nanosheets with thickness up to c.a. 2 nm, featured by fully accessible and highly interconnected pores, for boosting the H<sub>2</sub>S selective oxidation process. The PAM-0.3-700 sample has revealed an unprecedented desulfurization activity with sulfur formation rate of 1165 g<sub>sulfur</sub> kg<sub>cat</sub><sup>-1</sup> h<sup>-1</sup>, other than a remarkable stability (>80 h). Experimental and theoretical studies have unveiled the critical role of edge sites containing unpaired electrons and nitrogen species with respect to the material aptitude towards O<sub>2</sub> dissociation and HS<sup>-</sup> activation. The material in presence of a highly interconnected porous network facilitates the reactants/product diffusion especially for catalysis operated under harsh experimental conditions.

## 1. Introduction

Hydrogen sulfide (H<sub>2</sub>S) is recognized as the one of the most hazardous and smelly sulfur-containing gas deriving from a wide variety of industrial processes including industrial waste-gas streams, natural gas refineries, biogas purification and coal chemistry [1–3]. Its presence in pipelines is unacceptable because it is not only dangerous for human health but it is also corrosive towards equipment and infrastructures. Accordingly, flue gas streams need be properly treated as to match with the safety and ecological requirements linked to the abatement of their H<sub>2</sub>S content and its storage in the form of safety S-containing compounds. At present, the most widely used technology for removing H<sub>2</sub>S is based on the Claus process [2 H<sub>2</sub>S + SO<sub>2</sub> → (3/n) S<sub>n</sub> + 2 H<sub>2</sub>O], which converts H<sub>2</sub>S into the safer and useful elemental sulfur. However, a 3–5 % v/v of H<sub>2</sub>S remains in the gas tail because of thermodynamic limitations. Further gas tail purification is generally accomplished through

dry/wet adsorption, incineration or catalytic oxidation procedures [4–7]. The selective H<sub>2</sub>S oxidation to elemental sulfur using molecular oxygen as reactant [2 H<sub>2</sub>S + O<sub>2</sub> → (2/n) S<sub>n</sub> + 2 H<sub>2</sub>O] is a promising and low-cost approach that generally requires milder experimental conditions while offering high process efficiency [8,9].

Among the catalytic materials for H<sub>2</sub>S selective oxidation reaction, metal-free carbon catalysts have been extensively investigated because of their high thermal stability and good conductivity, porosity and unique structural features [10–12]. The manipulation of their surface chemical properties in terms of surface functional groups, defect engineering, or light heteroatoms, especially N, along with their ultimate morphology has been scrutinized as valuable carbocatalysts for selective oxidation of H<sub>2</sub>S [13–20]. Extraordinary, manipulation of structural defects on solid-state nanomaterials is crucial for the development of advanced catalytic materials with improved performance in selected transformations [21–23]. Thereinto, the coordination environment of

\* Corresponding author.

E-mail address: [yuefeng.liu@dicp.ac.cn](mailto:yuefeng.liu@dicp.ac.cn) (Y. Liu).

<sup>1</sup> These authors contributed equally in this work.

single atom metal catalysts [24,25] and electronic properties of supported metal nanoparticles [26,27] can be modulated as well as the electron delocalization over structural and topological defects of metal-free carbon nanomaterials can be enhanced [22,28]. For example, single-atom carbon-based materials (SACs) have also been prepared and reported as efficient hydrogen sulfide ( $\text{H}_2\text{S}$ ) selective oxidation catalysts. Authors demonstrated how the appropriate N-coordination sphere of single-atoms controls their performance in the oxidative desulfurization process [29–31]. In addition, ultra-high density of defective sites ( $2.46 \times 10^{13} \text{ cm}^{-2}$ ) in carbon-based nanomaterial is also known to

provide metal-free systems featuring with excellent oxygen reduction catalytic performance under both basic and acidic conditions [32]. However, the structural defects on carbon nanomaterials usually embedded in microporous channel may limit the exposure of the active sites hence resulting into systems with poor reagents accessibility.  $\text{H}_2\text{S}$  selective oxidation is a typical reaction where the elemental sulfur as product (generally in the form of  $\text{S}_8$  clusters) can be responsible of a progressive pore clogging. Its deposit can inhibit the interaction between reactants and active sites, especially for carbon nanomaterials with a large extent of micropores [33,34].

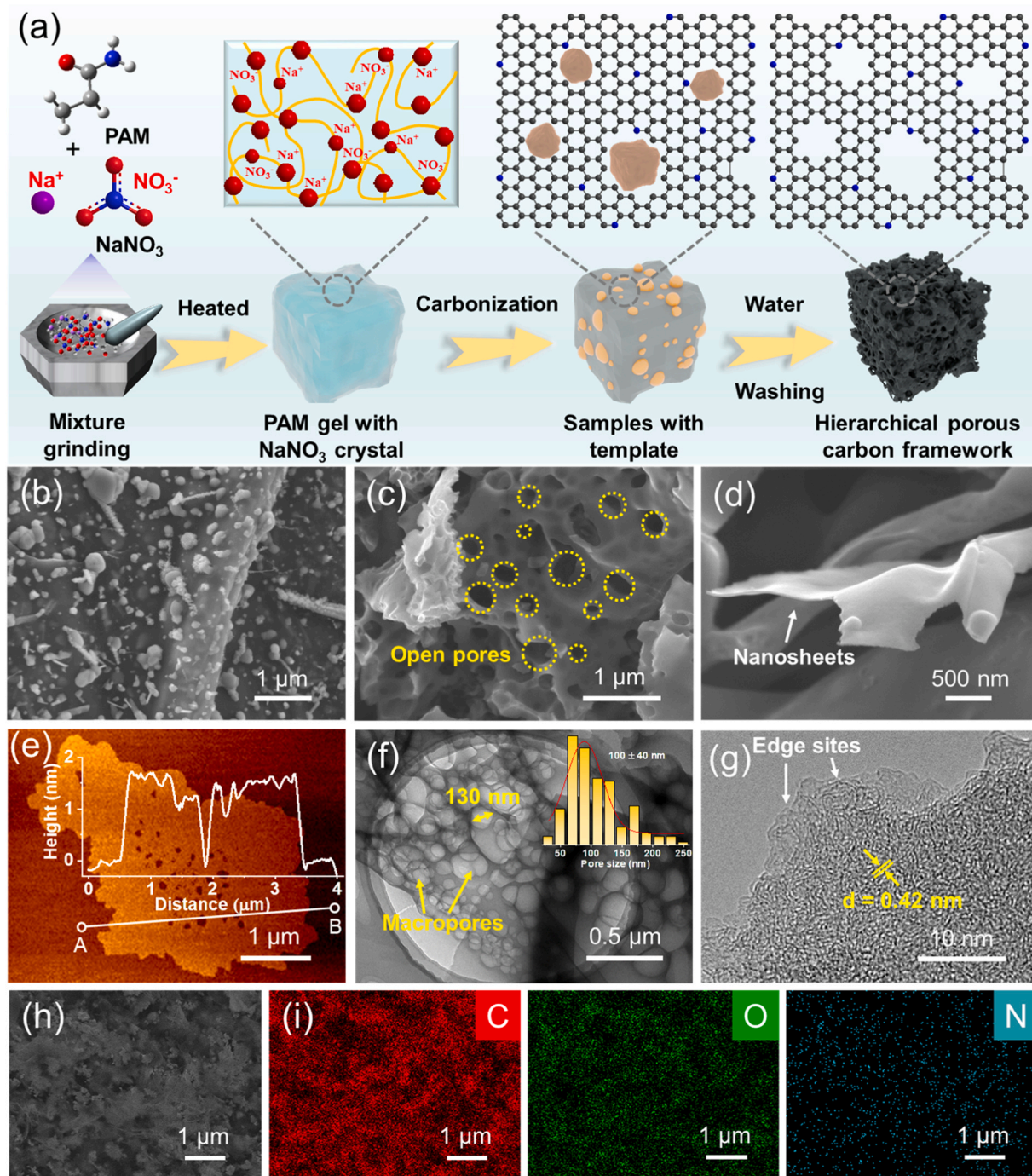


**Fig. 1.** The synthetic procedure and morphology analysis of defect-enriched N-doped C-nanosheets. (a) Synthetic illustration of the fabrication process for the carbocatalyst. SEM images of PAM-0.3–700 (b) before washing and (c) after washing removal of residual  $\text{Na}_2\text{O}$  template. (d) Magnified SEM image of PAM-0.3–700. (e) AFM image of PAM-0.3–700 with monolayer attachment and corresponding thickness along the line. (f) TEM image and (g) HR-TEM image of PAM-0.3–700. (h) SEM image and (i) elemental mapping images of PAM-0.3–700.

Designing fully accessible porous, N-doped C-based networks with a high density of active sites can give an answer to the need of carbocatalysts featured by high desulfurization activity. Their generally high surface area along with high accessibility to active sites within unique hierarchically porous structures, ensure rapid mass transport in the carbon matrix. N-doped carbon nanoflakes with abundant structural defects have proven to enhance significantly the catalytic H<sub>2</sub>S selective oxidation [35]. However, their current preparation routes typical include the use of various soft/hard templates, such as tetraethyl orthosilicate [36], MgO [37], CaO [38]. Most of these reagents are hazardous and costly chemicals, and strong acid (HF [36], HCl [39]) etching is generally required to remove templates during the material post-treatment hence limiting the facile synthesis of porous carbons. Therefore, the interconnected hierarchically porous carbon architecture synthesized through universal and green method to satisfy the above-mentioned properties still remains a great challenge.

Herein, we report a simple, eco-friendly and cheap protocol for the synthesis of interconnected hierarchically porous, N-defects-enriched, C-networks with tunable pore-structure using polyacrylamide (PAM) as a unique carbon and nitrogen source and NaNO<sub>3</sub> as a macro-/mesoporous sacrificial template/porogen. A schematic representation of the proposed synthetic methodology is outlined in Fig. 1a. The as-prepared porous N-doped carbons present relatively high specific surface areas and pore size distribution ideal to generate high desulfurization performance catalysts. A selected sample from this series has shown its superior desulfurization performance respect to other metal- and carbon-based catalysts of the *state-of-the-art*. It has shown a sulfur formation rate as high as 1165 g<sub>sulfur</sub> kg<sub>cat.</sub><sup>-1</sup> h<sup>-1</sup> at 210 °C when the desulfurization process was operated under high weight hourly space velocity (WHSV = 120 L g<sup>-1</sup> h<sup>-1</sup>). Overall, the results reported hereafter well-demonstrate the potentiality of interconnected hierarchically porous N-doped carbons prepared by our innovative approach and their practical application as cheap, highly efficient and durable catalysts for the challenging H<sub>2</sub>S selective oxidation in the natural gas desulfurization treatment.

## 2. Experimental section

### 2.1. Chemicals

The analytical grade sodium nitrate (NaNO<sub>3</sub>, 99 %) was purchased from Tianjin Kemiou Chemical Reagent Co., Ltd. Polyacrylamide ((C<sub>3</sub>H<sub>5</sub>NO)<sub>n</sub>) was purchased from Aladdin. The chemical reagents were used without further purification.

### 2.2. Preparation of the hierarchical N-doped porous carbon

In a typical process, the hierarchical N-doped porous carbocatalysts were prepared by a simple and gentle one-pot molten salt method. In details, 1 g of polyacrylamide (PAM) and an appropriate amount of NaNO<sub>3</sub> (from 0 to 0.5 NaNO<sub>3</sub>/PAM weight ratio) were mixed and finely grounded into a black powder submitted to pyrolysis in a tubular furnace to 400–800 °C for 4 h at a heating rate of 5 °C•min<sup>-1</sup> under 100 mL•min<sup>-1</sup> argon flow. After cooling to room temperature, the obtained black product was washed with a large amount of deionized water to remove Na<sup>+</sup> and other residues before being dried in an oven at 60 °C for 24 h to obtain the final products labeled as PAM-X-T where X is the NaNO<sub>3</sub>/PAM weight ratio and T is the annealing temperature). Furthermore, PAM-0.3-700-S and PAM-0.3-700-R represent the spent and regenerated sample of PAM-0.3-700, respectively.

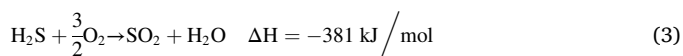
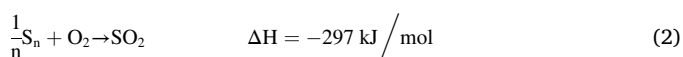
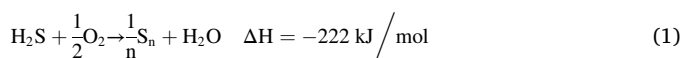
### 2.3. Characterization

The surface morphology of the N-doped hierarchically porous carbon catalysts was investigated using a JSM-7800F scanning electron microscope (SEM) with an energy dispersive X-ray (EDX) analyzer. The

microstructure of the catalysts was observed on a transmission electron microscope (TEM, JEM-2100). Atomic force microscopy (AFM) studies were carried out on a NanoWizard electron microscope. X-ray diffraction (XRD) analysis was conducted on a Bruker Advance D8 diffractometer with Cu Kα radiation. The Raman spectra were obtained by RENISHAW inVia Raman microscope (excitation wavelength of 532 nm and power of 5 mW). N<sub>2</sub> adsorption-desorption isotherm was obtained over an ASAP 2020 Micromeritics instrument and all samples were degassed at 350 °C for 10 h before the measurement. X-ray adsorption spectra (XAS) were measured at the beamline of the National Synchrotron Radiation Laboratory (NSRL) Soft X-ray Magnetic Circle Orientation Station (XMCD). Under a vacuum of more than 10<sup>-8</sup> Pa, the X-ray absorption near-edge structure (XANES) spectra of the C K-edge and N K-edge are obtained. X-ray photoelectron spectroscopy (XPS) data were obtained through an ESCALAB 250Xi with an Al Kα X-ray source (hν = 1486.6 eV). Elemental analyses were performed by using inductively coupled plasma-optical emission spectrometer (ICP-OES) using a PerkinElmer 7300DV.

### 2.4. Desulfurization measurements

The selective oxidation of H<sub>2</sub>S to sulfur over PAM-X-T catalysts was conducted in a continuous fixed-bed steel reactor under atmospheric pressure. The following reactions may occur in the oxidative desulfurization process (Eqs. (1)–(3)):



During the reaction process, 100 mg of catalysts were packed in the central section of a tubular reactor (inner diameter of 8 mm). The reaction temperature was controlled by two K-type thermocouples placed in the furnace and in the axial center of the reaction tube, respectively. A simulated gas containing 1 vol% of H<sub>2</sub>S, 2.5 vol% of O<sub>2</sub> and balanced He flows through the fixed bed at a total flow rate of 100 mL min<sup>-1</sup>. All gas flows were controlled by a mass flow controller. For parameter experiments, the weight hourly space velocity (WHSV) is specified in the range of 40,000 to 120,000 mL g<sup>-1</sup> h<sup>-1</sup>, the molar ratio of O<sub>2</sub>/H<sub>2</sub>S is set in the range of 1.5–2.5, and the steam concentration is in the range of 0–30 vol %. The steam is fed into the reactants by bubbling He gas through a deionized water containing a liquid saturator, kept at a fixed temperature. Air condenser and ice-water condenser are placed below the reactor to trap sulfur at the outlet. The concentration of the tail gases from the reactor was analyzed online by an Agilent 7890B gas chromatograph (GC) coupled with a thermal conductivity detector (TCD). The limit of the detection for the different gas is 400 pgs/mL.

The H<sub>2</sub>S conversion (X), sulfur selectivity (S) and sulfur formation rate in terms of mass (λ<sub>cat.</sub>) of catalyst were calculated according to (Eqs. (4)–(6)):

$$X_{\text{H}_2\text{S}} [\%] = \left( 1 - \frac{FC_{\text{H}_2\text{S}, \text{outlet}}}{F_0 C_{\text{H}_2\text{S}, \text{inlet}}} \right) \times 100 \quad (4)$$

$$S_s [\%] = \left( 1 - \frac{FC_{\text{SO}_2, \text{outlet}}}{F_0 C_{\text{H}_2\text{S}, \text{inlet}} - FC_{\text{H}_2\text{S}, \text{outlet}}} \right) \times 100 \quad (5)$$

$$\lambda_{\text{cat.}} [\text{g}_{\text{sulfur}} \text{kg}_{\text{cat.}}^{-1} \text{h}^{-1}] = \frac{F_0 \times X_{\text{H}_2\text{S}} \times S_s \times C_{\text{H}_2\text{S}, \text{inlet}}}{m_{\text{cat.}} \times t} \quad (6)$$

where F<sub>0</sub> and F are the inlet and outlet gas flow rates, C<sub>H<sub>2</sub>S</sub> and C<sub>SO<sub>2</sub></sub> stand for the concentration of H<sub>2</sub>S and SO<sub>2</sub>, m<sub>cat.</sub> represents the mass of catalyst.



## 2.5. DFT calculations

All structures in this work were performed using the Dmol3 program in Materials Studio 7.0. The Generalized gradient approximation (GGA) method with the Perdew-Burke-Ernzerhof (PBE) exchange-correlation functional [40,41] was selected. The H, C, N, O, and S were treated as in the all electron. The double numerical plus polarization (DNP) basis set was achieved ENREF 65 [42]. About the full geometric optimization, the convergence parameters were  $1.0 \times 10^{-6}$  Hartree for total energy, a smearing of 0.005 Hartree for orbital occupancy was used. The vibrational frequencies were calculated to confirm each stable intermediate or transition state.

To explore the activation of HS<sup>-</sup>, O<sub>2</sub> and desulfurization of key intermediates on defect-rich N-doped porous carbon, the models of single-layer graphene without defects and nitrogen doping, with nitrogen doping only, with defects only and with defects plus nitrogen doping were constructed, which are denoted as edged graphene (Edge-C), N-doped graphene (N-C), defect-modified graphene (D-C) and defect-modified N-doped graphene (N-D-C), respectively. The atomic positions were allowed to be relaxed without any symmetry constraint in all calculations.

## 3. Results and discussion

### 3.1. Synthesis and characterization of hierarchically porous and N-defects enriched C-nanosheets

Polyacrylamide (PAM) was used as the unique C, N source while NaNO<sub>3</sub> was employed as a sacrificial template/porogen for the control of the final interconnected porosity in the prepared N-doped C-networks (Fig. 1a). PAM was transformed into an aerogel upon grinding and heating it in the presence of NaNO<sub>3</sub>. Afterwards, the mixture was pyrolyzed under Ar atmosphere using a corundum crucible (Fig. S1). During pyrolysis, melt NaNO<sub>3</sub> (350 °C) formed a sticky gel with PAM and it started to decompose upon increasing the pyrolysis temperature (> 600 °C). NaNO<sub>3</sub> decomposition releases abundant volatiles (i.e., N<sub>2</sub>, O<sub>2</sub>, CO<sub>2</sub> and NO), which act as foam blowing agents in the control of the final porosity of N-doped carbon matrices.

Scanning electron microscopy (SEM) of PAM-0.3–700 has shown the presence of a large amount of Na<sub>2</sub>O particles on the unwashed catalyst (Fig. 1b and Fig. S2) resulting from the thermal decomposition of NaNO<sub>3</sub>. Open macropores indicated by orange circles (Fig. 1c) were then obtained on the same sample upon the etching of Na<sub>2</sub>O particles with simple deionized water (washing treatment). These results indicate that Na<sub>2</sub>O plays a key role in the control of the porous structure of final C-based samples. Furthermore, as SEM images show, all samples present a sheets-like morphology (Fig. 1d and Fig. S3, S4). The atomic force microscopy (AFM) conducted on the sample has allowed to characterize the average thickness of the layered N-doped carbons. As Fig. 1e shows, the height profile measured along the A-B line of a C, N-nanosheet highlights a thickness of about 2 nm which vertically consists of a mean of six nanosheets. Besides, small-sized mesopores and macropores can be observed in the wall of the nanosheet (Fig. 1e and S5). Due to the two-dimensional channel, there are more defective edges in the ultrathin nanosheet structure which can supply a high density of exposed active sites and facilitate the mass transport. The representative TEM image of PAM-0.3–700 in Fig. 1f further confirms that the porous structure is composed of numerous macropores with pore size between 60 and 150 nm and connected to the thin nanosheets around them. In addition, highly defective edge sites could be formed in the graphene layers upon addition of NaNO<sub>3</sub> salt and the annealing process can increase the defective edge sites (Fig. 1g). The SEM images and related energy-dispersive X-ray spectroscopy (EDS) elemental mapping of PAM-0.3–700 (Fig. 1h and i) reveal that the C, N, and O elements of the matrix are uniformly distributed.

N<sub>2</sub> physisorption analyses were conducted to study the specific

surface area and pore-size distribution of the as-prepared carbocatalysts. As shown in Fig. 2a, PAM-0–700 showed a type-III isotherm in line with the IUPAC classification, typical of a nonporous network with a low specific surface area (SSA 26 m<sup>2</sup> g<sup>-1</sup>). SSA increased significantly up to 3262 m<sup>2</sup> g<sup>-1</sup> upon the addition of NaNO<sub>3</sub> (Fig. 2a, Table S1) and the increase of the pyrolysis temperature (Fig. S6a). Pore size distribution curves indicated that all the samples showed similar morphologies featured by micro-meso-porous networks after NaNO<sub>3</sub> addition (Fig. 2b, Fig. S6b) [12,43].

For the sake of investigating the crystal and structural properties of the synthesized porous carbon materials, X-ray diffraction (XRD) and Raman spectroscopy analyses were conducted. As shown in Fig. 2c and S7, the samples exhibited a broad diffraction peak at 24° and an inconspicuous diffraction peak at 44° arising from the (002) and (100) lattice planes of graphite, respectively [44]. The (002) peak was gradually broadened until its disappearance while increasing the NaNO<sub>3</sub> content and pyrolysis temperature. This indicated a lower extent of graphitization and crystallinity of the sample and the generation of amorphous carbon networks [44,45].

Raman spectra can be deconvoluted into five components (Fig. 2d, Fig. S8): G peak (~1580 cm<sup>-1</sup>) was assigned to symmetric and crystalline sp<sup>2</sup> carbon, D<sub>1</sub> peak (~1350 cm<sup>-1</sup>) and D<sub>2</sub> peak (~1620 cm<sup>-1</sup>) were associated with the defects/edges in the in-plane of graphene layers and irregular graphitic lattice on the surface, D<sub>3</sub> peak (~1500 cm<sup>-1</sup>) was related to amorphous carbon and the D<sub>4</sub> peak (~1200 cm<sup>-1</sup>) was attributed to other polyenes and ionic impurities [46–48]. The intensity ratio of D<sub>1</sub> band to G band (I<sub>D1</sub>/I<sub>G</sub>) were 1.68 and 1.89 for PAM-0–700 and PAM-0.3–700, respectively, suggesting that more structural defects were generated upon the addition of NaNO<sub>3</sub>. For a better understanding of the influence of NaNO<sub>3</sub> and thermal treatments on the porous structure and chemical properties of the synthesized samples, NaNO<sub>3</sub>/PAM weight ratio and pyrolysis temperature were correlated to defect density (n<sub>D</sub>, cm<sup>-2</sup>) [46] and specific surface area. As displayed in Figs. 2e and 2f, the defect density (n<sub>D</sub>) and SSA increased by increasing both parameters. This trend indicated that the etching effect of NaNO<sub>3</sub> became more prominent upon increasing the pyrolysis temperature from 400 to 800 °C, creating more defective edge sites [49]. The schematic illustration of PAM-X-700 samples prepared by varying the amounts of NaNO<sub>3</sub> shows that the latter can reach the internal structure of carbon matrix for etching and then expand the size of pores (Fig. 2g).

Considering the relevant changes in the morphology of N-doped nanocarbons, synchrotron-based near-edge X-ray absorption fine structure (NEXAFS) of C K-edge and N K-edge have been exploited to elucidate the detailed chemical state of C and N in the samples. Peaks at 285.0, 287.9, 288.6 and 293.7 eV of C K-edge X-ray absorption structure (XAS) spectra were assigned to the 1s-π\* transition of C=C bond, the π\* feature of C-O and C=O bonds [50,51], and the σ\* (C=C) bonds [52], respectively (Fig. 3a, Fig. S12a). The distinctive peak at 284.9 eV was ascribed to defects in the carbon lattice, in particular divacancy and Stone-Wales defects containing pentagon [53,54]. PAM-0.3–700 showed a peak of stronger intensity at 284.9 eV respect to PAM-0–700 and PAM-0.3–400, indicating a higher defective-sites concentration. Fig. 3b and Fig. S12b shows the N K-edge XAS spectra. Peaks at 399.3, 402.8 and 407.8 eV were assigned to pyridinic N (Pyri N), pyrrolic N (Pyrr N) and graphitic N (Grap N) [50], respectively. Compared to PAM-0–700 and PAM-0.3–400, the intensity of these N species for PAM-0.3–700 decreased except for the pyridinic N species.

Inspired by the XANES analysis, the surface elemental composition and bonding configurations of the N-doped porous carbons were resolved by XPS measurements. The XPS survey spectra (Fig. S9) - in accord with the results from SEM elemental mapping - have revealed the presence of C, N, and O elements. To assess the amount of residual Na, ICP-OES experiment was conducted and the result showed that the Na content of the PAM-0.3–700 sample was as low as 0.04 wt% (Table S7). No signals related to Na species were detected on the materials' surface from XPS survey spectra, indicating the complete removal of the pristine



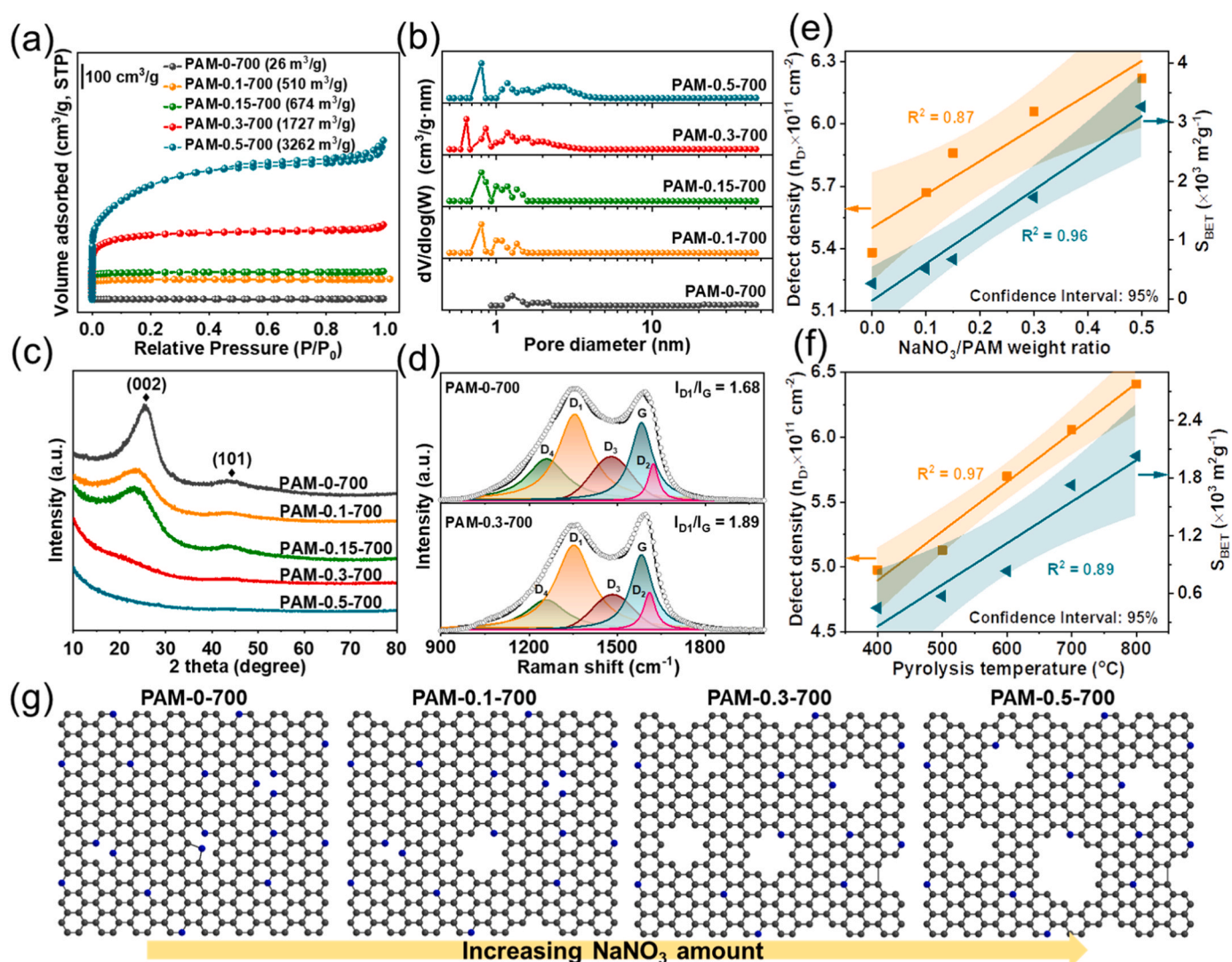


**Fig. 2.** Structure evolution of N-doped C-nanosheets. (a) N<sub>2</sub> adsorption-desorption isotherm curves and (b) pore size distribution of the N-doped nanocarbons synthesized with different NaNO<sub>3</sub> content. (c) XRD patterns of N-doped nanocarbons with different NaNO<sub>3</sub> content. (d) Raman spectra of the obtained N-doped nanocarbons. Defect density (calculated by Cançado's equation [46]) and BET specific surface area as a function of (e) the weight ratio of NaNO<sub>3</sub> to PAM and (f) pyrolysis temperature. (g) A schematic representation of the structure evolution of N-doped nanocarbons for PAM-X-700 samples when varying the amount of NaNO<sub>3</sub> salt.

sacrificial porogen/template and its solid decomposition products. N-content decreased from 7.3 to 1.1 at% when the amount of NaNO<sub>3</sub> salt increased. On the other hand, N-content decreased from 6.0 to 2.9 at% while increasing of the pyrolysis temperature from 400 to 800 °C [55, 56]. These data highlight the influence of NaNO<sub>3</sub> salt on the surface composition of the carbocatalysts. The C 1s spectra of the samples can be deconvoluted into five characteristic peaks (Fig. S10), which belonging to sp<sup>2</sup>-hybridized C=C graphite-like carbon (C1, 284.8 eV), unsaturated carbon structures including C-N and C-O (C2, 286.4 eV), C=O (C3, 287.4 eV), -COO bonds (C4, 288.9 eV) as well as the shake-up π-π\* transition of carbon (C5, 290.7 eV), respectively. It can be seen in Table S2 that there are mainly two kinds of carbon configurations presented in the porous carbon, which are sp<sup>2</sup>-hybridized and unsaturated carbon. Chemical states of the O atoms were also analyzed. The O content of samples after addition of NaNO<sub>3</sub> are lower than that of PAM-0-700 without NaNO<sub>3</sub> addition, which may result from the removal of oxygen functional groups during heat process with NaNO<sub>3</sub> (Table S3). As displayed in Fig. S11, the high-resolution O 1s XPS spectrum could be well deconvoluted into three peaks corresponding to C=O (O1) at ~532.4 eV, O-C=O (O2) at ~533.6 eV, and C-O (O3) at

~534.9 eV. As shown on Fig. 3c,d, high-resolution XPS confirms the presence of N-containing species including pyridinic (Pyri N, 398.5 eV), pyrrolic (Pyrr N, 400.2 eV), graphitic (or quaternary) nitrogen (Grap N, 401.8 eV), and nitrogen oxides (Oxid N, 403.6 eV) [57,58]. Previous studies from the literature have revealed that more reactive N-species were located at the edge of the graphitic plane in the form of pyridinic, pyrrolic and oxidized nitrogen groups [59–61]. Notably, the percentage of N atoms on the edge of carbon planes (Pyri N, Pyrr N, and Oxid N from 81 % to 95 %, Fig. 3e, Table S4) was much higher than N-species present in the carbon lattice (Grap N). This was indicative of a higher amount of potentially active sites in the samples prepared with our NaNO<sub>3</sub>-assisted method.

### 3.2. H<sub>2</sub>S-to-S<sub>8</sub> catalytic oxidation performance with PAM-X-T samples

The desulfurization performance of the newly synthesized and porous N-doped C-nanosheets were initially investigated in a fixed-bed reactor at 210 °C and a weight hourly space velocity (WHSV) of 40000 mL g<sup>-1</sup> h<sup>-1</sup>. As shown in Fig. 4a, PAM-0-700 exhibited an extremely low H<sub>2</sub>S conversion (only 14.1 %). Samples prepared under

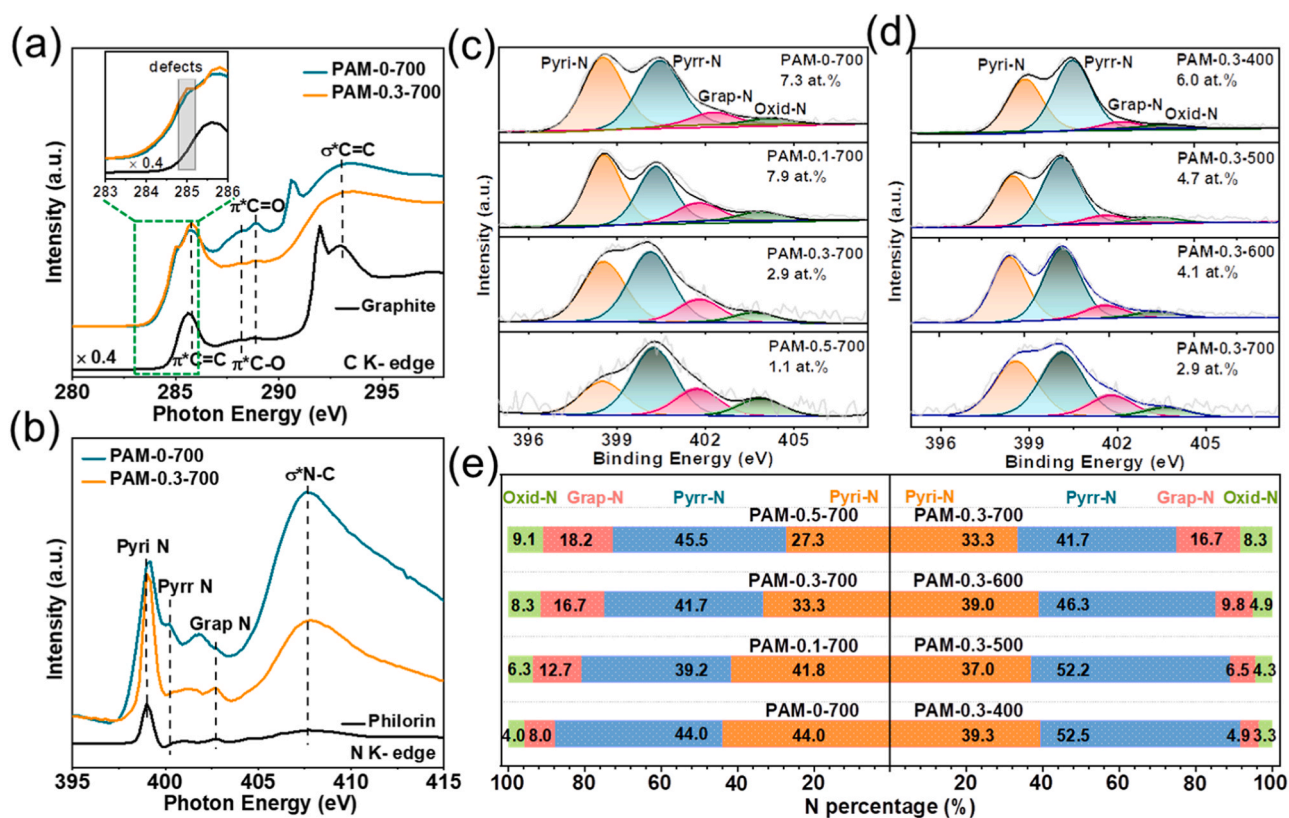


Fig. 3. Chemical composition of the N-doped C-nanosheets. (a) C K-edge and (b) N K-edge XANES spectra. (c, d) High-resolution N 1s XPS spectra and (e) the contents of different nitrogen species of porous N-doped nanocarbon.

the same pyrolysis temperature but in the presence of  $\text{NaNO}_3$  as template/porogen showed significantly enhanced  $\text{H}_2\text{S}$  conversions values up to 95.9 % with a sulfur selectivity over 75 % (PAM-0.3-700 prepared with a  $\text{NaNO}_3/\text{PAM}$  weight ratio of 0.3). Higher  $\text{NaNO}_3$  contents neither increased  $\text{H}_2\text{S}$  conversion nor resulted in higher selectivity in the desulfurization process. With PAM-0.5-700, sulfur selectivity dropped down to 70 %. It can be inferred that the increased surface area and N-edge defect density (Fig. 2e) hold a critical effect on the ultimate catalysts performance with respect to the  $\text{H}_2\text{S}$ -to- $\text{S}_8$  selective oxidation. When N-content was too low (1.1 at% for PAM-0.5-700) the process selectivity decreased in spite of an almost doubled sample SSA (Fig. 2a, PAM-0.3-700 vs. PAM-0.5-700). As far as the influence of the pyrolysis temperature is concerned, Fig. 4b shows that  $\text{H}_2\text{S}$  conversion gradually increased while increasing the samples pyrolysis temperature (from 400 to 600 °C) and remained almost stable for samples prepared up to 800 °C. At the same time, the sulfur selectivity decreased when pyrolysis temperature increased in the same range of values. As a result, sulfur formation rate ( $\lambda_{\text{cat}}$ ) was  $112 \text{ g}_{\text{sulfur}} \text{ kg}_{\text{cat}}^{-1} \text{ h}^{-1}$  on PAM-0-700 and grew up to its maximum value on PAM-0.3-600 ( $691 \text{ g}_{\text{sulfur}} \text{ kg}_{\text{cat}}^{-1} \text{ h}^{-1}$ ), with an increase up to 6.2 times with respect to the former sample (Fig. 4c). These results demonstrate that PAM-X-T catalytic performance in the selective  $\text{H}_2\text{S}$ -to- $\text{S}_8$  oxidation correlated closely with the starting content of  $\text{NaNO}_3$  as well as with the adopted pyrolysis conditions. Accordingly, catalytic outcomes recorded with this new class of porous materials were the result of a delicate balance between their morphological (SSA and pore distribution) and chemico-physical properties (N-content and defects density). Remarkably, PAM-0.3-700 showed to be an exceptionally performing  $\text{H}_2\text{S}$ -to- $\text{S}_8$  catalyst under extremely high WHSV (up to  $120,000 \text{ mL g}^{-1} \text{ h}^{-1}$ ) with a sulfur formation rate up to  $1165 \text{ g}_{\text{sulfur}} \text{ kg}_{\text{cat}}^{-1} \text{ h}^{-1}$  (Fig. 4d). This result outperforms all previously reported desulfurization catalysts, including metal-based ( $\gamma\text{-Al}_2\text{O}_3$ ,  $\text{CeO}_2\text{-R}$ ,  $\text{Co@NC-4}$ ,  $\text{CUS-MIL-100(Fe)}$ , etc) [4,62–66] and carbon-based systems (N-CNT, PCNUC5, ppy-KOH-700, NPC700, N-HLCF-800, etc) of

the state-of-the-art [6,9,11,12,14,17,19,20,34,67–71].

PAM-0.3-700 was then selected as the catalyst of choice for studying the effects of other reaction parameters such as operative temperature, WHSV, steam and  $\text{O}_2/\text{H}_2\text{S}$  molar ratio with respect to its desulfurization performance. The catalyst performance was recorded at each temperature value after reaching the steady state conditions and the results are presented in Fig. 5a. Increasing the reaction temperature from 130 to 230 °C resulted in a dramatic increase of  $\text{H}_2\text{S}$  conversion that reached about 100 % at 230 °C. However, sulfur selectivity decreased steadily from 91.2 % to 71.5 % likely due to the formation of hot spots at the catalytic bed thus favoring the occurrence of undesired over-oxidation paths [74]. As shown in Fig. 5a, sulfur yield registered with PAM-0.3-700 enhanced gradually while increasing the reaction temperature till exhibiting its best value ( $\sim 74.1$  %) at 210 °C before decreasing its activity for higher temperature values (230 °C).

Fig. 5b shows the evolution of the catalyst activity and selectivity upon varying the reagents weight hourly space velocity (WHSV) at the operative temperature of 210 °C. As expected, nearly 97.7 % of  $\text{H}_2\text{S}$  conversion was obtained under lower WHSV ( $40,000 \text{ mL g}^{-1} \text{ h}^{-1}$ ). Then, it decreased down to 83.2 % at the higher WHSV values ( $120,000 \text{ mL g}^{-1} \text{ h}^{-1}$ ) as a consequence of reduced reactants/catalyst contact times. On the other hand, an enhancement of sulfur selectivity from 77.4 % to 82.6 % was observed when the reaction was operated under higher space velocity. This effect was basically ascribed to a faster removal of the produced elemental sulfur from the catalyst surface, hence hampering the occurrence of over-oxidation paths. The relationship between the WHSV and the sulfur formation rate (at 210 °C) is outlined in Fig. 5c. The increase of WHSV from 40,000 to  $120,000 \text{ mL g}^{-1} \text{ h}^{-1}$  resulted in a significant increase of the sulfur formation rate. This trend confirmed the beneficial role of the highly porous morphology of PAM-derived catalysts that favored an ideal reagents and sulfur mass transport throughout the catalyst channels.

Water vapor was then added to the reactants mixture to investigate



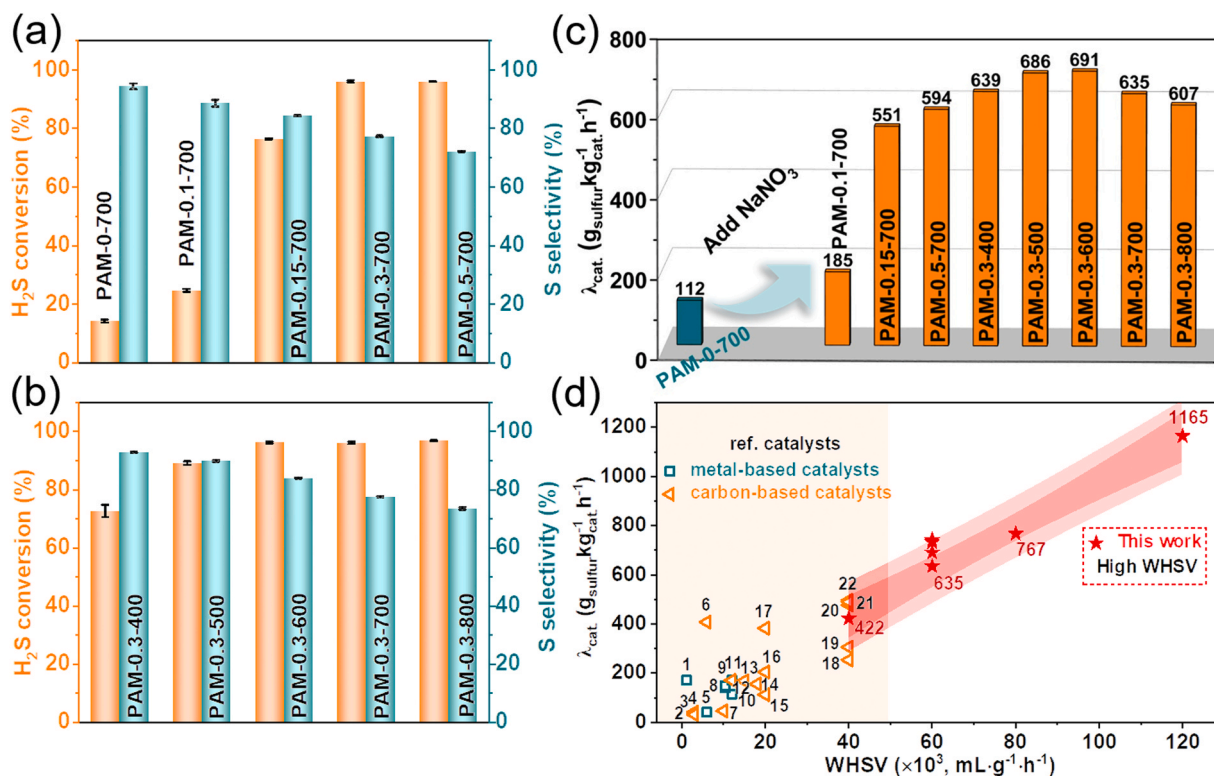


**Fig. 4.** Catalytic performance of as-prepared carbocatalysts for H<sub>2</sub>S selective oxidation. (a, b) H<sub>2</sub>S conversion and S selectivity, (c) corresponding sulfur formation rate of N-doped porous carbocatalysts with various salt contents and pyrolysis temperatures. Reaction conditions: T = 210 °C, WHSV = 40,000 mL g<sup>-1</sup> h<sup>-1</sup>, H<sub>2</sub>O content = 30 vol%, O<sub>2</sub>-to-H<sub>2</sub>S molar ratio = 2.5. (d) Comparison of different desulfurization catalysts reported in the literature and the sulfur formation rate of PAM-0.3-700. (1) Fe<sub>2</sub>O<sub>3</sub>/γ-Al<sub>2</sub>O<sub>3</sub> (Ref. [62]); (2) CNU-p600 (Ref. [72]); (3) CNM-600 (Ref. [9]); (4) PCNUC5 (Ref. [67]); (5) 8FeCe (Ref. [63]); (6) ppy-KOH-700 (Ref. [68]); (7) N-CNT beads (Ref. [11]); (8) γ-Al<sub>2</sub>O<sub>3</sub> (Ref. [64]); (9) CeO<sub>2</sub>-R (Ref. [4]); (10) Co@NC-4 (Ref. [65]); (11) CUS-MIL-100(Fe) (Ref. [66]); (12) N-HLCF-800 (Ref. [69]); (13) NPC-8 (Ref. [34]); (14) N-OMCS-700 (Ref. [17]); (15) N-CNT/SiC foam (Ref. [19]); (16) N-CNT (ref. [19]); (17) <sup>A</sup>N@C/SiC<sub>2</sub> (Ref. [70]); (18) O-CNT-250-24 (Ref. [73]); (19) N@CF-800 (Ref. [71]); (20) N-C/CNT-2 %P (Ref. [20]); (21) N-C/CNT<sub>500</sub> (Ref. [6]); (22) NPC700 (Ref. [12]).

the influence of steam on the selective catalytic oxidation of H<sub>2</sub>S at 210 °C. As depicted in Fig. 5d, H<sub>2</sub>S conversion and S selectivity measured under anhydrous condition, decreased from about 97.9 % and 77.9–95.1 % and 75.2 %, respectively, when the process was operated in the presence of 10 vol% steam. A further increase of the steam content (up to 30 vol%) did not result into any appreciable change of the PAM-0.3-700 catalytic performance, hence indicating a good catalyst resistance to higher contents of water vapors.

The effect of different O<sub>2</sub>/H<sub>2</sub>S molar ratio on the desulfurization performance of PAM-0.3-700 was also studied at 210 °C. As shown in Fig. 5e, when O<sub>2</sub>/H<sub>2</sub>S molar ratio increased from 1.5 to 2.5, H<sub>2</sub>S conversion grew slightly from 92.5 % to 96.0 % while sulfur selectivity decreased from 85.1 % to 77.2 %. These data highlight the good aptitude of PAM-0.3-700 to generate active oxygen species even under reduced O<sub>2</sub> partial pressures, that is known to promote the over oxidation of the formed elemental sulfur and H<sub>2</sub>S to SO<sub>2</sub> [63].

The catalyst durability on run is another critical parameter to take into account while evaluating practical use of newly synthesized catalytic materials in the challenging H<sub>2</sub>S-to-S<sub>8</sub> selective oxidation. As illustrated in Fig. 5f, PAM-0.3-700 showed excellent stability at 210 °C. The H<sub>2</sub>S conversion decreased gradually from 100 % to 93.1 % throughout the long-term test (80 h) while sulfur selectivity slightly increased from 80.2 % to 82.9 %. This moderate decrease of activity was ascribed to a moderate but progressive sulfur deposition on the catalyst active sites. The PAM-0.3-700 catalyst recovered at the end of the long-term catalytic cycle (PAM-0.3-700-S) underwent further characterization by XRD, SEM and corresponding EDS elemental mapping as well as TEM. Based on the XRD pattern, graphite crystal planes were almost unchanged (Fig. S16). The morphology of PAM-0.3-700-S (Fig. S17 and Fig. S18) did not change appreciably with respect to its fresh counterpart

(PAM-0.3-700). At the same time, EDS mapping (Fig. S19) showed the presence of large sulfur deposits on the carbon network. XPS measurements were also performed to clarify the chemical composition of species at the PAM-0.3-700-S (S = spent) and PAM-0.3-700-R (R = regenerated) surface. In accord with EDS mapping, Fig. S20a showed S 2s and S 2p signals attributed to sulfur deposits on the spent PAM-0.3-700-S catalyst. For the S 2p spectrum in Fig. S20b, two former peaks are related to S<sub>n</sub> (S 2p<sub>3/2</sub> at 163.48 eV and S 2p<sub>1/2</sub> at 164.67 eV) with a total content of 93.85 %, while the peak located at 168.39 eV comes from the presence of sulfate generated by the H<sub>2</sub>S over-oxidation path [7,73]. The sulfur content of the spent PAM-0.3-700-S catalyst was 10.9 at%, and that of the regenerated PAM-0.3-700-R catalyst decreased to 1.6 at%. This indicated that sulfur deposits were mostly removed from the catalyst surface after the thermal treatment under inert gas (Table S5). The total N content decreased to 2.1 at% in the spent catalyst and then increased to 2.6 at% after regeneration process. As shown in Fig. 5g and S15, the H<sub>2</sub>S conversion rate and selectivity of regenerated catalyst (PAM-0.3-700-R) could be fully recovered (96.6 % H<sub>2</sub>S conversion of 96.6 % and sulfur selectivity of 82.8 %).

### 3.3. On the origin of the enhanced desulfurization performance of PAM-0.3-700

To further elucidate the outstanding performance of PAM-0.3-700 in the catalytic H<sub>2</sub>S-to-S<sub>8</sub> process, the intrinsic kinetics of the N-doped carbocatalyst were studied in detail. Fig. S21 shows the Arrhenius plots measuring the effect of the reaction temperature on the catalytic H<sub>2</sub>S oxidation rate of PAM-0-700 and PAM-0.3-700. The apparent activation energy for PAM-0.3-700 was 78.2 kJ/mol, whereas it was almost doubled (143.7 kJ/mol) in the case of PAM-0-700. It could be



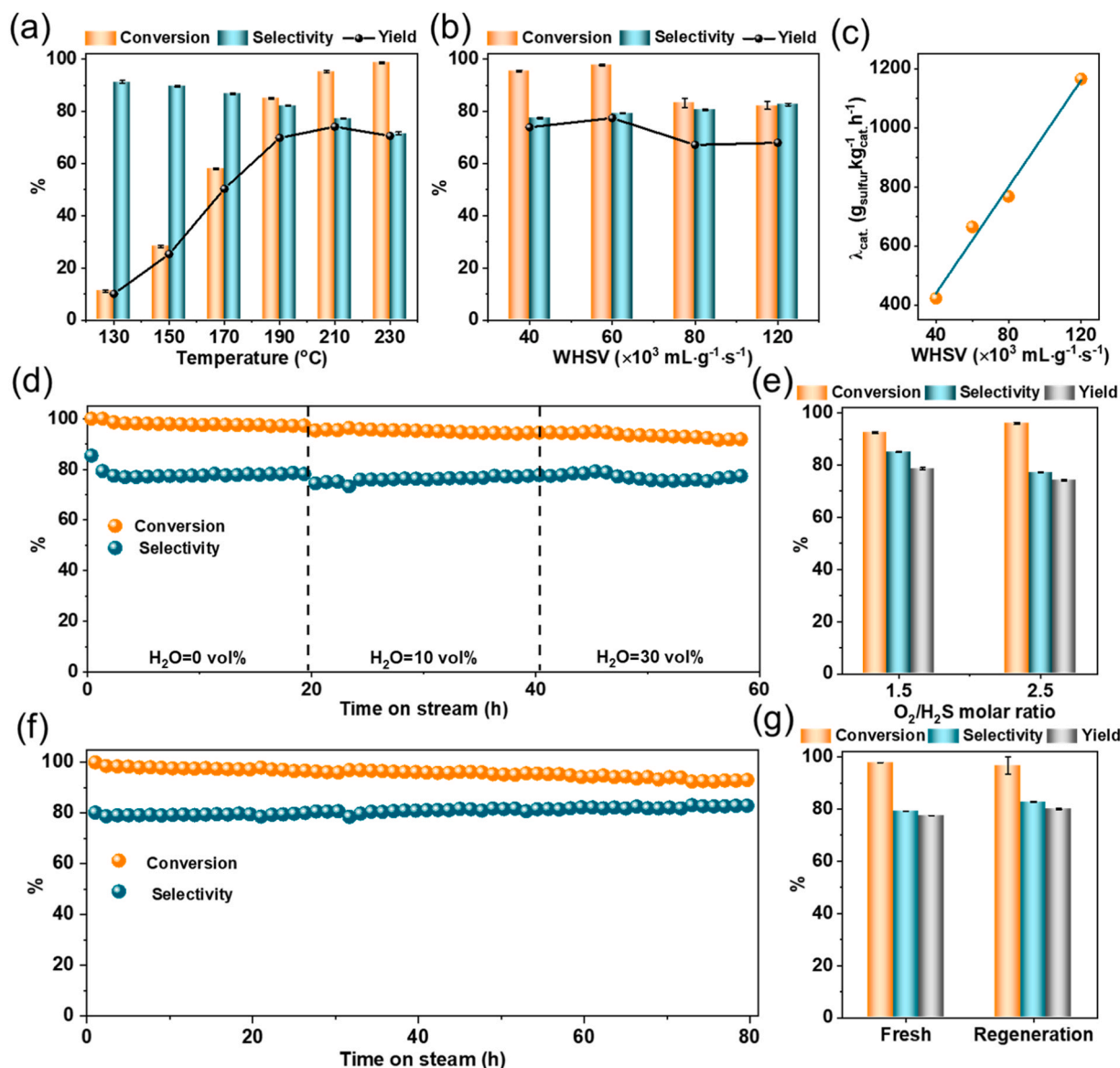


**Fig. 5.** Reaction parameter of H<sub>2</sub>S selective oxidation towards industrial application. (a) Effect of reaction temperature on H<sub>2</sub>S selective oxidation performance over PAM-0.3-700. Reaction conditions: WHSV = 40,000 mL g<sup>-1</sup> h<sup>-1</sup>, O<sub>2</sub>-to-H<sub>2</sub>S molar ratio = 2.5. Effect of Weight Hourly Space Velocity (WHSV) on (b) the desulfurization performance and (c) the sulfur formation rates over PAM-0.3-700. Reaction conditions: T = 210 °C, O<sub>2</sub>-to-H<sub>2</sub>S molar ratio = 2.5. (d) Effect of H<sub>2</sub>O content on the desulfurization performance over PAM-0.3-700. Reaction conditions: T = 210 °C, WHSV = 40,000 mL g<sup>-1</sup> h<sup>-1</sup> and O<sub>2</sub>-to-H<sub>2</sub>S molar ratio = 2.5, steam concentration = 0, 10 and 30 vol%. (e) Effect of the O<sub>2</sub>-to-H<sub>2</sub>S molar ratio on the desulfurization performance over PAM-0.3-700. Reaction conditions: T = 210 °C, WHSV = 40,000 mL g<sup>-1</sup> h<sup>-1</sup>. (f) Stability performance of H<sub>2</sub>S selective oxidation over PAM-0.3-700. Reaction conditions: T = 210 °C, WHSV = 40,000 mL g<sup>-1</sup> h<sup>-1</sup>, O<sub>2</sub>-to-H<sub>2</sub>S molar ratio = 2.5. (g) Comparison of the desulfurization performance of fresh and regenerated PAM-0.3-700.

concluded that the addition of NaNO<sub>3</sub> as a template/porogen in the synthesis of porous, N-defect enriched C-nanosheets increased the H<sub>2</sub>S conversion. Subsequently, we investigated the effects of partial pressures of O<sub>2</sub> and H<sub>2</sub>S on the reaction rate at a reaction temperature as low as 140 °C (Fig. S22 and Table S6). As shown in Fig. S22, the reaction rate of H<sub>2</sub>S increased significantly upon increasing O<sub>2</sub> and H<sub>2</sub>S partial pressures and the reaction order for O<sub>2</sub> and H<sub>2</sub>S were calculated as 1.25 and 0.66, respectively. In accord with previously reported data on carbon-based catalysts employed for the H<sub>2</sub>S-to-S<sub>8</sub> selective oxidation [75], the higher reaction order for O<sub>2</sub> respect to H<sub>2</sub>S indicate that O<sub>2</sub> activation and dissociation were critical steps in the process [76,77].

DFT calculations have finally been used to unveil the lower energy barrier associated to the O<sub>2</sub> activation on the highly defective PAM-0.3-700 catalyst respect to its non-porous PAM-0-700 counterpart (Fig. 6). The *in-silico* modeling has demonstrated that molecular oxygen

can be activated more easily on PAM-0.3-700 than on PAM-0-700, thus accounting for the superior catalytic performance of the former in the selective H<sub>2</sub>S oxidation process. The DFT study indicated that edge-N sites in the highly defective C-nanosheets promoted O<sub>2</sub> activation and increased the amount of dissociated oxygen species thus boosting the materials performance in the desulfurization reaction.

As shown in Fig. S23, we constructed four types of computational models, i.e., undoped (Edge-C), and N-doped edged graphene (N-C), defect-enriched undoped (D-C) and N-doped graphene (N-D-C) frameworks. The introduction of heteroatoms or defects in the sp<sup>2</sup> carbon lattice is known to break the electroneutrality of the C-network and modify the charge/spin material distribution, resulting into samples with improved catalytic performance [78,79]. The redistributed charges on the van der Waals surface have frequently been used to predict the reaction active sites [80,81]. Therefore, we analyzed the electron

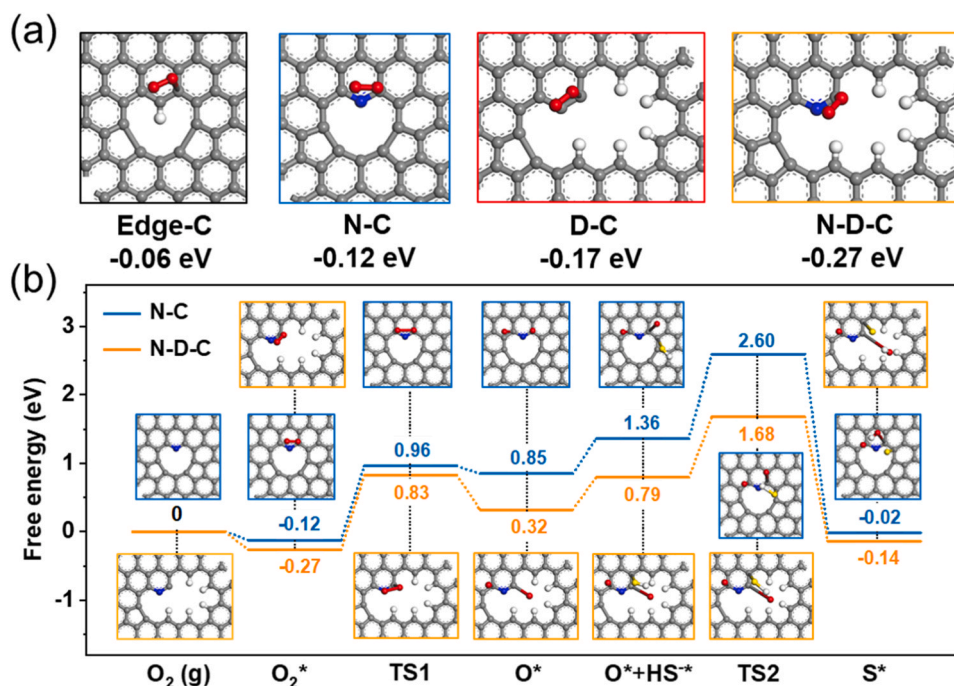


**Fig. 6.** Mechanism study of the active sites over as-prepared carbocatalyst. (a) The adsorption energy that  $O_2$  chemisorption on the Edge-C, N-C, D-C and N-D-C surface. (b) Calculated free energy diagram of  $H_2S$  selective oxidation reaction on N-C and N-D-C with the corresponding structures along the reaction paths. Colours code in the scheme: C atom is grey, N atom is blue, O atom is red, S atom is yellow, H atom is white.

density distribution on the above four models to provide a more intuitive analysis. As displayed in Fig. S24a, the charge distribution at the edge-C network was pretty uniform. However, when N species and defects were present, then the charge distribution was altered (Fig. S24b-d). Two extremum values were found around the pyridinic N atom and the C defect neighboring the heteroelement, suggesting that electron-rich material portions were formed. The altered charge distribution indicated that edge-N sites were responsible for reagents activation (i.e.,  $O_2$  and  $HS^*$ ). The adsorption and activation of molecular  $O_2$  were then crucial steps in the  $H_2S$  selective oxidation. To explore the role of edge-N sites, the molecular adsorption and dissociation of  $O_2$  was investigated on all proposed molecular models, Edge-C, N-C, D-C and N-D-C. The  $O_2$  molecular adsorption geometries are shown in Fig. 6a. The calculated adsorption energy between  $O_2$  and N-doped porous carbon were  $-0.06$  eV (Edge-C),  $-0.12$  eV (N-C),  $-0.17$  eV (D-C) and  $-0.27$  eV (N-D-C), respectively, indicating that  $O_2$  adsorption was weak on Edge-C, N-C (without defect) and D-C (without Nitrogen) models. Hence, the coexistence of N species and defects was very important for the  $O_2$  activation in accord to the observed poor activity of PAM-0-700 catalyst (Fig. 4a, Fig. S13a). Both experimental and theoretical studies indicated the existence of a synergistic effect between edge defect and N species for the control of the materials performance in the catalytic  $H_2S$  selective oxidation reaction.

We have further evaluated the reaction mechanism and the influence of the above-mentioned synergistic effect on the reaction pathway. As shown in Fig. 6b and Fig. S25-S26, the reaction started with the dissociative adsorption of molecular  $O_2$  to give the  $O^*$  species adsorbed at the carbon site neighboring N, via a transition state (TS1) with an activation barrier of 1.09, 1.08, 1.14 and 1.09 eV for Edge-C, N-C, D-C and N-D-C, respectively. Then,  $HS^*$  species were adsorbed near the C-O group with a calculated energy barrier on N-D-C much lower than that calculated on Edge-C, N-C and D-C (0.88 eV vs 1.43, 1.24 and 1.38 eV). These results indicated that Edge-C, N-C and D-C were not favorable for  $HS^*$  oxidation whereas N-D-C model was an efficient candidate for promoting this fundamental step. All these data taken together lead to the conclusion that N-D-C model synergistically combined the effect of nitrogen doping

with that of edge-site defects within a catalyst featured by relatively low activation barriers for reagents and thus with an intrinsically high aptitude to act as a  $H_2S$  desulfurization system.

Accordingly, a promising strategy for the development of optimal desulfurization catalysts based on defective-edges N-doped porous carbon networks is proposed. Accordingly, a simplified model of the fabricated material is outlined in Fig. 7a. As confirmed by AFM (Fig. 1e) and TEM images (Fig. 1f), carbon nanosheets present several through-holes including pore opening, pore blockage, pore narrowing and pore misalignment as detailed in Fig. 7b. The effect of pore structure (i.e., pore size distribution) on dynamics of reagents ( $H_2S$  and  $O_2$ ) and products (polysulfides,  $S_2$ ,  $S_4$ ,  $S_6$  and  $S_8$  molecules) are depicted in Fig. 7c. Fig. 7d shows the geometric dimension of  $S_8$  molecule. The diameter of  $S_8$  is calculated to be 8.06 Å (the radius of the molecule), which is close to the mean size of the micropores ( $\approx 1$  nm). Thus, micropores of carbon, which confine and prevent the transfer of the large  $S_8$  molecules (Fig. 7c-II) at longer transfer pathway, allow the transfer of small  $S_2$ ,  $S_4$  and  $S_6$  molecules (Fig. 7c-I) at short transfer pathway. For mesopores, in which the pore size is much larger than that of the polysulfides, the latter can be easily transported through the pores, as shown in Fig. 7c-III. Due to the thickness of the carbon nanosheets (about 2 nm) and the high density of through-holes in the N, C-network, polysulfides can be transported fast through the short transfer passway.

Realizing the highly efficient and selective conversion of  $H_2S$  to elemental sulfur requires catalysts with both a high exposure of active sites and short transfer paths for the mass diffusion during the reaction. Overall, this study sheds light on important catalyst features for the design and synthesis of more and more active and selective metal-free systems to be employed in the challenging purification/abatement of  $H_2S$  contaminants from natural gas tails.

#### 4. Conclusion

In summary, we have proposed a straightforward, cheap and highly reproducible methodology for the synthesis of tunable, hierarchically porous, N-defect enriched C-nanosheets using a  $NaNO_3$ -assisted

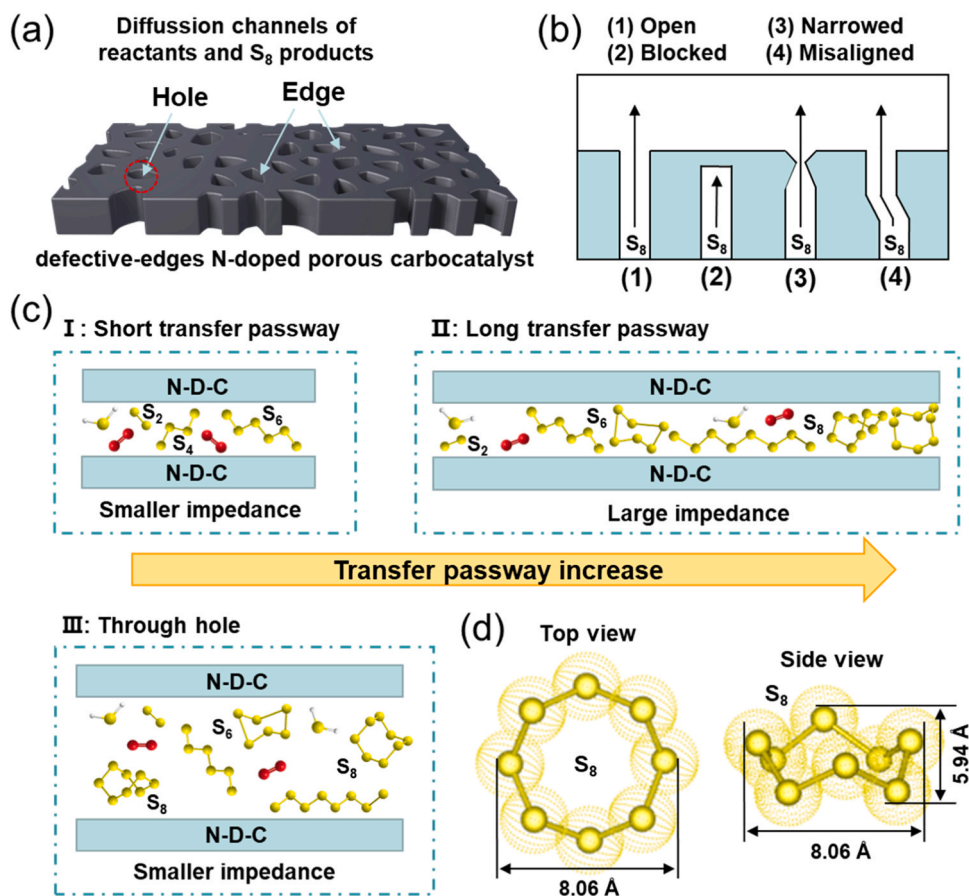


**Fig. 7.** Illustration of sulfur cluster diffusion during the reaction. (a) Illustration of the fabricated defective-edges N-doped porous carbocatalyst. (b) Surface pore structures including pore opening, pore blockage, pore narrowing and pore misalignment. (c) the transfer processes of the reactants ( $H_2S$  and  $O_2$ ) and products (polysulfides,  $S_2$ ,  $S_4$ ,  $S_6$  and  $S_8$  molecules) in different types of porous structure: I, a short transfer pathway in microporous carbon; II, a long transfer pathway in microporous carbon; III, mesoporous carbon. (d) Theoretical calculation of the dimensions of polysulfides ( $S_8$ ).

pyrolysis of commercial polyacrylamide (PAM) as the C- and N-source. The proposed protocol gives rise to C, N-nanosheets with a high-density of defective edge-sites and an average thickness of isolated flakes around 2 nm. Among the isolated metal-free systems, PAM-0.3–700 showed the highest performance in the selective  $H_2S$ -to- $S_8$  oxidation process with a sulfur formation rate up to  $1165 \text{ g}_{\text{sulfur}} \cdot \text{kg}_{\text{cat}}^{-1} \cdot \text{h}^{-1}$  when the desulfurization process was operated under high WHSV ( $120,000 \text{ mL g}^{-1} \text{ h}^{-1}$ ). This catalyst largely outperforms other metal and carbon-based systems reported in the literature so far. The origin of such a high catalytic performance was disclosed by the combination of experimental and DFT simulation studies. We demonstrated how the presence of a high-density of edge-N sites combined with highly porous and interconnected C-networks facilitated the material mass transport (reagents and product dynamics), boosting at the same time  $O_2$  dissociation and  $HS^-$  oxidation processes. The as-prepared N-defects enriched C-nanosheets represent a novel class of highly porous materials with unique potentialities as metal-free catalysts for the  $H_2S$  selective oxidation in the challenging and industrially relevant purification/treatment of natural gas tails.

#### CRediT authorship contribution statement

Y.L. conceived and supervised this work. S.L. and X.Z. performed the experiments, collected the data, and wrote the paper. H.F. conducted the DFT calculations. X.L., G.T., G.G. and C. P.-H. helped with data analyses and discussions. G.G. and Y.L. revised the paper. All authors contributed to editing the paper.

#### Declaration of Competing Interest

The authors declare that they have no known competing financial interests or personal relationships that could have appeared to influence the work reported in this paper.

#### Data availability

Data will be made available on request.

#### Acknowledgement

This work was financially supported by the National Key R&D Program of China (No. 2022YFC3701900), National Natural Science Foundation of China (Nos. 21606243, 21972140 and 22172161), Liaoning Revitalization Talents Program (XLYC1907053) and Dalian National Laboratory for Clean Energy (DNL202021). Y. L. and G. G. finally thank the CAS President's International Fellowship Initiative (PIFI) program for support. XAS experiments were conducted at the MCD Endstation at the BL12B-a beamline in the National Synchrotron Radiation Laboratory (NSRL) in Hefei, China.

#### Appendix A. Supporting information

Supplementary data associated with this article can be found in the online version at [doi:10.1016/j.apcatb.2023.123505](https://doi.org/10.1016/j.apcatb.2023.123505).



## References

- [1] T. Bostelaar, V. Vitvitsky, J. Kumutima, B.E. Lewis, P.K. Yadav, T.C. Brunold, M. Filipovic, N. Lehnert, T.L. Stemmler, R. Banerjee, Hydrogen sulfide oxidation by myoglobin, *J. Am. Chem. Soc.* 138 (2016) 8476–8488.
- [2] X. Zhang, Y. Tang, N. Qiao, Y. Li, S. Qu, Z. Hao, Comprehensive study of H<sub>2</sub>S selective catalytic oxidation on combined oxides derived from Mg/Al-V<sub>10</sub>O<sub>28</sub> layered double hydroxides, *Appl. Catal. B* 176–177 (2015) 130–138.
- [3] C. Duong-Viet, J.-M. Nhut, T. Truong-Huu, G. Tuci, L. Nguyen-Dinh, Y. Liu, C. Pham, G. Giambastiani, C. Pham-Huu, A nitrogen-doped carbon-coated silicon carbide as a robust and highly efficient metal-free catalyst for sour gas desulfurization in the presence of aromatics as contaminants, *Catal. Sci. Technol.* 10 (2020) 5487–5500.
- [4] X. Zheng, Y. Li, L. Zhang, L. Shen, Y. Xiao, Y. Zhang, C. Au, L. Jiang, Insight into the effect of morphology on catalytic performance of porous CeO<sub>2</sub> nanocrystals for H<sub>2</sub>S selective oxidation, *Appl. Catal. B* 252 (2019) 98–110.
- [5] X. Zhang, Y. Tang, S. Qu, J. Da, Z. Hao, H<sub>2</sub>S-selective catalytic oxidation: catalysts and processes, *ACS Catal.* 5 (2015) 1053–1067.
- [6] S. Li, Y. Liu, H. Gong, K.-H. Wu, H. Ba, C. Duong-Viet, C. Jiang, C. Pham-Huu, D. Su, N-doped 3D mesoporous carbon/carbon nanotubes monolithic catalyst for H<sub>2</sub>S selective oxidation, *ACS Appl. Nano Mater.* 2 (2019) 3780–3792.
- [7] J. Wang, C. Ke, X. Jia, C. Ma, X. Liu, W. Qiao, L. Ling, Polyethyleneimine-functionalized mesoporous carbon nanosheets as metal-free catalysts for the selective oxidation of H<sub>2</sub>S at room temperature, *Appl. Catal. B* 283 (2021), 119650.
- [8] C. Yang, H. Ye, J. Byun, Y. Hou, X. Wang, N-rich carbon catalysts with economic feasibility for the selective oxidation of hydrogen sulfide to sulfur, *Environ. Sci. Technol.* 54 (2020) 12621–12630.
- [9] L. Shen, G. Lei, Y. Fang, Y. Cao, X. Wang, L. Jiang, Polymeric carbon nitride nanomesh as an efficient and durable metal-free catalyst for oxidative desulfurization, *Chem. Commun.* 54 (2018) 2475–2478.
- [10] S. Bashkova, F.S. Baker, X. Wu, T.R. Armstrong, V. Schwartz, Activated carbon catalyst for selective oxidation of hydrogen sulphide: on the influence of pore structure, surface characteristics, and catalytically-active nitrogen, *Carbon* 45 (2007) 1354–1363.
- [11] H. Ba, C. Duong-Viet, Y. Liu, J.-M. Nhut, P. Granger, M.J. Ledoux, C. Pham-Huu, Nitrogen-doped carbon nanotube spheres as metal-free catalysts for the partial oxidation of H<sub>2</sub>S, *C. R. Chim.* 19 (2016) 1303–1309.
- [12] C. Xu, J. Chen, S. Li, Q. Gu, D. Wang, C. Jiang, Y. Liu, N-doped honeycomb-like porous carbon derived from biomass as an efficient carbocatalyst for H<sub>2</sub>S selective oxidation, *J. Hazard. Mater.* 403 (2021), 123806.
- [13] F. Sun, J. Liu, H. Chen, Z. Zhang, W. Qiao, D. Long, L. Ling, Nitrogen-rich mesoporous carbons: highly efficient, regenerable metal-free catalysts for low-temperature oxidation of H<sub>2</sub>S, *ACS Catal.* 3 (2013) 862–870.
- [14] C. Duong-Viet, Y. Liu, H. Ba, L. Truong-Phuoc, W. Baaziz, L. Nguyen-Dinh, J.-M. Nhut, C. Pham-Huu, Carbon nanotubes containing oxygenated decorating defects as metal-free catalyst for selective oxidation of H<sub>2</sub>S, *Appl. Catal. B* 191 (2016) 29–41.
- [15] M.A. Patel, F. Luo, M.R. Khoshi, E. Rabie, Q. Zhang, C.R. Flach, R. Mendelsohn, E. Garfunkel, M. Szostak, H. He, P-doped porous carbon as a metal free catalyst for selective aerobic oxidation with an unexpected mechanism, *ACS Nano* 10 (2016) 2305–2315.
- [16] S. Li, Q. Gu, N. Cao, Q. Jiang, C. Xu, C. Jiang, C. Chen, C. Pham-Huu, Y. Liu, Defect enriched N-doped carbon nanoflakes as robust carbocatalysts for H<sub>2</sub>S selective oxidation, *J. Mater. Chem. A* 8 (2020) 8892–8902.
- [17] X. Kan, X. Chen, W. Chen, J. Mi, J.-Y. Zhang, F. Liu, A. Zheng, K. Huang, L. Shen, C. Au, L. Jiang, Nitrogen-decorated, ordered mesoporous carbon spheres as high-efficient catalysts for selective capture and oxidation of H<sub>2</sub>S, *ACS Sustain. Chem. Eng.* 7 (2019) 7609–7618.
- [18] X. Liu, G.Q. Zhangsun, Y. Zheng, S.J. Liang, Y.N. Cao, F.J. Liu, Y.H. Xiao, L. L. Jiang, Hierarchical N-doped carbons endowed with structural base sites toward highly selective adsorption and catalytic oxidation of H<sub>2</sub>S, *Ind. Eng. Chem. Res.* 60 (2021) 2101–2111.
- [19] K. Chizari, A. Deneuve, O. Ersen, I. Florea, Y. Liu, D. Edouard, I. Janowska, D. Begin, C. Pham-Huu, Nitrogen-doped carbon nanotubes as a highly active metal-free catalyst for selective oxidation, *ChemSusChem* 5 (2012) 102–108.
- [20] C. Xu, Q. Gu, S. Li, J. Ma, Y. Zhou, X. Zhang, C. Jiang, C. Pham-Huu, Y. Liu, Heteroatom-doped monolithic carbocatalysts with improved sulfur selectivity and impurity tolerance for H<sub>2</sub>S selective oxidation, *ACS Catal.* 11 (2011) 8591–8604.
- [21] D.S. Su, S. Perathoner, G. Centi, Nanocarbons for the development of advanced, *Catal., Chem. Rev.* 113 (2013) 5782–5816.
- [22] Y. Jia, X. Yao, Defects in carbon-based materials for electrocatalysis: synthesis, recognition, and advances, *Acc. Chem. Res.* 56 (2023) 948–958.
- [23] X. Wang, Y. Jia, X. Mao, L. Zhang, D. Liu, L. Song, X. Yan, J. Chen, D. Yang, J. Zhou, K. Wang, A. Du, X. Yao, A directional synthesis for topological defect in carbon, *Chem* 6 (2020) 2009–2023.
- [24] X. Rong, H.J. Wang, X.L. Lu, R. Si, T.B. Lu, Controlled synthesis of a vacancy-defect single-atom catalyst for boosting CO<sub>2</sub> electroreduction, *Angew. Chem.* 132 (2020) 1977–1981.
- [25] F.S. Hage, G. Radtke, D.M. Kepaptsoglou, M. Lazzari, Q.M. Ramasse, Single-atom vibrational spectroscopy in the scanning transmission electron microscope, *Science* 367 (2020) 1124–1127.
- [26] W. Huang, A.C. Johnston-Peck, T. Wolter, W.-C.D. Yang, L. Xu, J. Oh, B.A. Reeves, C. Zhou, M.E. Holtz, A.A. Herzing, A.M. Lindenberg, M. Mavrikakis, M. Cargnello, Steam-created grain boundaries for methane C–H activation in palladium catalysts, *Science* 373 (2021) 1518–1523.
- [27] Z. Yang, W. Lai, B. He, J. Wang, F. Yu, Q. Liu, M. Liu, S. Zhang, W. Ding, Z. Lin, H. Huang, Tailoring interfacial chemistry of defective carbon-supported Ru catalyst toward efficient and CO-tolerant alkaline hydrogen oxidation reaction, *Adv. Energy Mater.* 13 (2023) 2300881.
- [28] Y. Jia, L. Zhang, L. Zhuang, H. Liu, X. Yan, X. Wang, J. Liu, J. Wang, Y. Zheng, Z. Xiao, E. Taran, J. Chen, D. Yang, Z. Zhu, S. Wang, L. Dai, X. Yao, Identification of active sites for acidic oxygen reduction on carbon catalysts with and without nitrogen doping, *Nat. Catal.* 2 (2019) 688–695.
- [29] G. Lei, W. Zhao, L. Shen, S. Liang, C. Au, L. Jiang, Isolated iron sites embedded in graphitic carbon nitride (g-C<sub>3</sub>N<sub>4</sub>) for efficient oxidative desulfurization, *Appl. Catal. B* 267 (2020), 118663.
- [30] G. Lei, Y. Tong, L. Shen, F. Liu, Y. Xiao, W. Lin, Y. Zhang, C. Au, L. Jiang, Highly active and sulfur-resistant Fe–N<sub>4</sub> sites in porous carbon nitride for the oxidation of H<sub>2</sub>S into elemental sulfur, *Small* 16 (2020) 2003904.
- [31] G. Lei, Y. Tong, L. Shen, Y. Zheng, S. Liang, W. Lin, F. Liu, Y. Cao, Y. Xiao, L. Jiang, Highly poison-resistant single-atom Co–N<sub>4</sub> active sites with superior operational stability over 460 h for H<sub>2</sub>S catalytic oxidation, *Small* 17 (2021) 2104939.
- [32] Q. Wu, Y. Jia, Q. Liu, X. Mao, Q. Guo, X. Yan, J. Zhao, F. Liu, A. Du, X. Yao, Ultra-dense carbon defects as highly active sites for oxygen reduction catalysis, *Chem* 8 (2022) 2715–2733.
- [33] Q. Chen, Z. Wang, D. Long, X. Liu, L. Zhan, X. Liang, W. Qiao, L. Ling, Role of pore structure of activated carbon fibers in the catalytic oxidation of H<sub>2</sub>S, *Ind. Eng. Chem. Res.* 49 (2010) 3152–3159.
- [34] X. Zhang, C. Xu, S. Li, X. Liu, Y. Liu, N-doped porous carbocatalyst engineering via modulating the crystalline size of ZIF-8 for continuous H<sub>2</sub>S selective oxidation, *Appl. Mater. Today* 25 (2021), 101228.
- [35] M. Sun, X. Wang, Y. Li, Z. Zhao, J. Qiu, Integration of desulfurization and lithium–sulfur batteries enabled by amino-functionalized porous carbon nanofibers, *Energy Environ. Mater.* 6 (2023), e12349.
- [36] S. Wang, J. Qin, Y. Zhao, L. Duan, J. Wang, W. Gao, R. Wang, C. Wang, M. Pal, Z.-S. Wu, W. Li, D. Zhao, Ultrahigh surface area N-doped hierarchically porous carbon for enhanced CO<sub>2</sub> capture and electrochemical energy storage, *ChemSusChem* 12 (2019) 3541–3549.
- [37] K. Xie, X. Qin, X. Wang, Y. Wang, H. Tao, Q. Wu, L. Yang, Z. Hu, Carbon nanocages as supercapacitor electrode materials, *Adv. Mater.* 24 (2012) 347–352.
- [38] C. Tang, B.-Q. Li, Q. Zhang, L. Zhu, H.-F. Wang, J.-L. Shi, F. Wei, CaO-templated growth of hierarchical porous graphene for high-power lithium-sulfur battery applications, *Adv. Funct. Mater.* 26 (2016) 577–585.
- [39] X.Y. Chen, C. Chen, Z.J. Zhang, D.H. Xie, Nitrogen-doped porous carbon spheres derived from polyacrylamide, *Ind. Eng. Chem. Res.* 52 (2013) 12025–12031.
- [40] J.P. Perdew, J.A. Chevary, S.H. Vosko, K.A. Jackson, M.R. Pederson, D.J. Singh, C. Fiolhais, Atoms, molecules, solids, and surfaces: applications of the generalized gradient approximation for exchange and correlation, *Phys. Rev. B* 46 (1992) 6671–6687.
- [41] J. Perdew, K. Burke, M. Ernzerhof, Generalized gradient approximation made simple, *30 Phys. Rev. Lett.* 77 (1996) 3865–3868.
- [42] B. Delley, An all-electron numerical method for solving the local density functional for polyatomic molecules, *J. Chem. Phys.* 92 (1990) 508–517.
- [43] H.-Y. Li, C. Li, Y.-Y. Wang, W.-D. Dong, X.-K. Zhang, M.-H. Sun, Y. Li, B.-L. Su, Pore structure unveiling effect to boost lithium-selenium batteries: selenium confined in hierarchically porous carbon derived from aluminum based MOFs, *Chem. Synth.* 3 (2023) 1–17.
- [44] Q. Wang, J. Yan, Y. Wang, G. Ning, Z. Fan, T. Wei, J. Cheng, M. Zhang, X. Jing, Template synthesis of hollow carbon spheres anchored on carbon nanotubes for high rate performance supercapacitors, *Carbon* 52 (2013) 209–218.
- [45] D. Puthusseri, V. Aravindan, B. Anothumakool, S. Kurungot, S. Madhavi, S. Ogale, From waste paper basket to solid state and Li-HEC ultracapacitor electrodes: a value added journey for shredded office paper, *Small* 10 (2014) 4395–4402.
- [46] L.G. Cançado, A. Jorio, E.H.M. Ferreira, F. Stavale, C.A. Achete, R.B. Capaz, M.V. O. Moutinho, A. Lombardo, T.S. Kulmala, A.C. Ferrari, Quantifying defects in graphene via raman spectroscopy at different excitation energies, *Nano Lett.* 11 (2011) 3190–3196.
- [47] A. Sadezky, H. Muckenhuber, H. Grothe, R. Niessner, U. Pöschl, Raman microspectroscopy of soot and related carbonaceous materials: spectral analysis and structural information, *Carbon* 43 (2005) 1731–1742.
- [48] R. Huang, J. Wang, B. Zhang, K.-H. Wu, Y. Zhang, D.S. Su, Phosphorus oxide clusters stabilized by carbon nanotubes for selective isomerization and dehydrogenation of  $\beta$ -isopentene, *Catal. Sci. Technol.* 8 (2018) 1522–1527.
- [49] Y. Wang, H. Liu, K. Wang, S. Song, P. Tsiakaras, 3D interconnected hierarchically porous N-doped carbon with NH<sub>3</sub> activation for efficient oxygen reduction reaction, *Appl. Catal. B* 210 (2017) 57–66.
- [50] H. Wei, Y. Ma, J. Luo, K.-H. Wu, W. Xie, G. Wen, C.-L. Chiang, W. Yan, S. Perathoner, G. Centi, Y. Liu, Creation of N–C=O active groups on N-doped CNT as an efficient CarboCatalyst for solvent-free aerobic coupling of benzylamine, *Carbon* 170 (2020) 338–346.
- [51] S.C. Ray, Z.N. Tetana, R. Erasmus, W.-F. Pong, N.J. Coville, Nitrogen-doped carbon spheres: an X-ray absorption near-edge structure spectroscopy study, *Appl. Phys. A* 115 (2014) 153–157.
- [52] S.C. Ray, C.W. Pao, J.W. Chiou, H.M. Tsai, J.C. Jan, W.F. Pong, R. McCann, S. S. Roy, P. Papakonstantinou, J.A. McLaughlin, Electronic properties of a-CN<sub>x</sub> thin films: an x-ray-absorption and photoemission spectroscopy study, *J. Appl. Phys.* 98 (2005).
- [53] W. Hua, B. Gao, S. Li, H. Ågren, Y. Luo, X-ray absorption spectra of graphene from first-principles simulations, *Phys. Rev. B* 82 (2010), 155433.

- [54] J. Wang, J. Zhou, Y. Hu, T. Regier, Chemical interaction and imaging of single  $\text{Co}_3\text{O}_4$ /graphene sheets studied by scanning transmission X-ray microscopy and X-ray absorption spectroscopy, *Energy Environ. Sci.* 6 (2013) 926–934.
- [55] K. Friedel Ortega, R. Arrigo, B. Frank, R. Schlögl, A. Trunschke, Acid–base properties of N-doped carbon nanotubes: a combined temperature-programmed desorption, X-ray photoelectron spectroscopy, and 2-propanol reaction investigation, *Chem. Mater.* 28 (2016) 6826–6839.
- [56] D. Wu, W. Song, L. Chen, X. Duan, Q. Xia, X. Fan, Y. Li, F. Zhang, W. Peng, S. Wang, High-performance porous graphene from synergetic nitrogen doping and physical activation for advanced nonradical oxidation, *J. Hazard. Mater.* 381 (2020), 121010.
- [57] J. Long, X. Xie, J. Xu, Q. Gu, L. Chen, X. Wang, Nitrogen-doped graphene nanosheets as metal-free catalysts for aerobic selective oxidation of benzylic alcohols, *ACS Catal.* 2 (2012) 622–631.
- [58] Z.H. Sheng, L. Shao, J.J. Chen, W.J. Bao, F.B. Wang, X.H. Xia, Catalyst-free synthesis of nitrogen-doped graphene via thermal annealing graphite oxide with melamine and its excellent electrocatalysis, *ACS Nano* 5 (2011) 4350–4358.
- [59] D.-W. Wang, F. Li, L.-C. Yin, X. Lu, Z.-G. Chen, I.R. Gentle, G.Q. Lu, H.-M. Cheng, Nitrogen-doped carbon monolith for alkaline supercapacitors and understanding nitrogen-induced redox transitions, *Chem. Eur. J.* 18 (2012) 5345–5351.
- [60] C.-M. Chen, Q. Zhang, X.-C. Zhao, B. Zhang, Q.-Q. Kong, M.-G. Yang, Q.-H. Yang, M.-Z. Wang, Y.-G. Yang, R. Schlögl, D.S. Su, Hierarchically aminated graphene honeycombs for electrochemical capacitive energy storage, *J. Mater. Chem.* 22 (2012) 14076–14084.
- [61] H. Chen, M. Zhou, Z. Wang, S. Zhao, S. Guan, Rich nitrogen-doped ordered mesoporous phenolic resin-based carbon for supercapacitors, *Electrochim. Acta* 148 (2014) 187–194.
- [62] W. Zhao, X. Zheng, S. Liang, X. Zheng, L. Shen, F. Liu, Y. Cao, Z. Wei, L. Jiang, Fe-doped  $\gamma\text{-Al}_2\text{O}_3$  porous hollow microspheres for enhanced oxidative desulfurization: facile fabrication and reaction mechanism, *Green Chem.* 20 (2018) 4645–4654.
- [63] X. Zheng, Y. Li, Y. Zheng, L. Shen, Y. Xiao, Y. Cao, Y. Zhang, C. Au, L. Jiang, Highly efficient porous  $\text{Fe}_x\text{Ce}_{1-x}\text{O}_2$  with three-dimensional hierarchical nanoflower morphology for  $\text{H}_2\text{S}$ -selective oxidation, *ACS Catal.* 10 (2020) 3968–3983.
- [64] L. Shen, X. Zheng, G. Lei, X. Li, Y. Cao, L. Jiang, Hierarchically porous  $\gamma\text{-Al}_2\text{O}_3$  nanosheets: Facile template-free preparation and reaction mechanism for  $\text{H}_2\text{S}$  selective oxidation, *Chem. Eng. J.* 346 (2018) 238–248.
- [65] Y. Liu, C. Song, Y. Wang, W. Cao, Y. Lei, Q. Feng, Z. Chen, S. Liang, L. Xu, L. Jiang, Rational designed Co@N-doped carbon catalyst for high-efficient  $\text{H}_2\text{S}$  selective oxidation by regulating electronic structures, *Chem. Eng. J.* 401 (2020), 126038.
- [66] X. Zheng, L. Zhang, Z. Fan, Y. Cao, L. Shen, C. Au, L. Jiang, Enhanced catalytic activity over MIL-100(Fe) with coordinatively unsaturated  $\text{Fe}^{2+}/\text{Fe}^{3+}$  sites for selective oxidation of  $\text{H}_2\text{S}$  to sulfur, *Chem. Eng. J.* 374 (2019) 793–801.
- [67] G. Lei, Z. Dai, Z. Fan, X. Zheng, Y. Cao, L. Shen, Y. Xiao, C. Au, L. Jiang, Porous nanosheets of carbon-conjugated graphitic carbon nitride for the oxidation of  $\text{H}_2\text{S}$  to elemental sulfur, *Carbon* 155 (2019) 204–214.
- [68] X. Liu, G. Zhangsun, Y. Zheng, S. Liang, Y. Cao, F. Liu, Y. Xiao, L. Jiang, Hierarchical N-doped carbons endowed with structural base sites toward highly selective adsorption and catalytic oxidation of  $\text{H}_2\text{S}$ , *Ind. Eng. Chem. Res.* 60 (2021) 2101–2111.
- [69] G. Zhang, Q. Zhu, W. Zhang, Y. Zheng, Y. Cao, S. Liang, Y. Xiao, F. Liu, L. Jiang, Efficiently integrated desulfurization from natural gas over Zn-ZIF-derived hierarchical Lamellar carbon frameworks, *Inorg. Chem.* 61 (2022) 6083–6093.
- [70] H. Ba, Y. Liu, L. Truong-Phuoc, C. Duong-Viet, X. Mu, W.H. Doh, T. Tran-Thanh, W. Baaziz, L. Nguyen-Dinh, J.-M. Nhut, I. Janowska, D. Begin, S. Zafeiratos, P. Granger, G. Tuci, G. Giambastiani, F. Banhart, M.J. Ledoux, C. Pham-Huu, A highly N-doped carbon phase “dressing” of macroscopic supports for catalytic applications, *Chem. Commun.* 51 (2015) 14393–14396.
- [71] Y. Liu, C. Duong-Viet, J. Luo, A. Hébraud, G. Schlatter, O. Ersen, J.-M. Nhut, C. Pham-Huu, One-pot synthesis of a nitrogen-doped carbon composite by electrospinning as a metal-free catalyst for oxidation of  $\text{H}_2\text{S}$  to sulfur, *ChemCatChem* 7 (2015) 2957–2964.
- [72] G. Lei, Y. Cao, W. Zhao, Z. Dai, L. Shen, Y. Xiao, L. Jiang, Exfoliation of graphitic carbon nitride for enhanced oxidative desulfurization: a facile and general strategy, *ACS Sustain. Chem. Eng.* 7 (2019) 4941–4950.
- [73] C. Duong-Viet, Y. Liu, H. Ba, L. Truong-Phuoc, W. Baaziz, L. Nguyen-Dinh, J.-M. Nhut, C. Pham-Huu, Carbon nanotubes containing oxygenated decorating defects as metal-free catalyst for selective oxidation of  $\text{H}_2\text{S}$ , *Appl. Catal. B* 191 (2016) 29–41.
- [74] C. Lei, W. Zhou, L. Shen, X. Zheng, Q. Feng, Y. Liu, Y. Lei, S. Liang, D. Zhang, L. Jiang, K. Zhou, Enhanced selective  $\text{H}_2\text{S}$  oxidation performance on  $\text{Mo}_2\text{C}$ -modified  $\text{g-C}_3\text{N}_4$ , *ACS Sustain. Chem. Eng.* 7 (2019) 16257–16263.
- [75] M. Steijns, F. Derks, A. Verloop, P. Mars, The mechanism of the catalytic oxidation of hydrogen sulfide: II. Kinetics and mechanism of hydrogen sulfide oxidation catalyzed by sulfur, *J. Catal.* 42 (1976) 87–95.
- [76] Y. Shen, G. Lu, Y. Guo, Y. Wang, Y. Guo, X. Gong, Study on the catalytic reaction mechanism of low temperature oxidation of CO over  $\text{Pd-Cu-Cl}_x/\text{Al}_2\text{O}_3$  catalyst, *Catal. Today* 175 (2011) 558–567.
- [77] Q. Gu, R. Huang, C. Xu, S. Li, S. Perathoner, G. Centi, Y. Liu, Nanodiamond derived N-doped  $\text{sp}^3/\text{sp}^2$  hybrid carbocatalysts for the aerobic oxidative synthesis of 2-substituted benzoxazoles, *Chem. Synth.* 3 (2023) 21.
- [78] C. Tang, Q. Zhang, Nanocarbon for oxygen reduction electrocatalysis: dopants, edges, and defects, *Adv. Mater.* 29 (2017), 1604103.
- [79] D. Li, Y. Jia, G. Chang, J. Chen, H. Liu, J. Wang, Y. Hu, Y. Xia, D. Yang, X. Yao, A defect-driven metal-free electrocatalyst for oxygen reduction in acidic electrolyte, *Chem* 4 (2018) 2345–2356.
- [80] P. Politzer, P.R. Laurence, K. Jayasuriya, Molecular electrostatic potentials: an effective tool for the elucidation of biochemical phenomena, *Environ. Health Perspect.* 61 (1985) 191–202.
- [81] P. Sjöberg, P. Politzer, Use of the electrostatic potential at the molecular surface to interpret and predict nucleophilic processes, *J. Phys. Chem.* 94 (1990) 3959–3961.